UDK 620.193.2
Original scientific article/Izvirni znanstveni članek

ISSN 1580-2949
Mater. Tehnol.

SOIL CORROSION MECHANISM AND CORROSION RATE MODEL FOR LONG-DISTANCE PIPELINE JOINTS IN THE R-K REGION OF CHAD

MEHANIZEM KOROZIJE ZARADI ZEMELJINE NA SPOJIH NAFTNIH CEVOVODOV V AFRIŠKI DRŽAVI ČAD IN RAZVOJ USTREZNEGA MODELA KOROZIJE

Lei Liu[1,#], Liang Ma[1,#], Haibin Han[2], Chao Zhang[3,#], Zhen Du[3], Zhenhuan Zhang[3], Minggang Li[3], Yanpeng Cao[4,#], Chenglei Liu[4,*], Weilong Liu[4]

[1]CNPC International (Chad) Co., Ltd.
[2]China National Oil and Gas Exploration and Development Company Ltd.
[3]China Petroleum Pipeline Engineering Co., Ltd.
[4]China Petroleum Pipeline Inspection Technologies Co., Ltd
# These authors contributed equally to this work and should be considered as co-first authors.

Prejem rokopisa – received: 2024-11-16; sprejem za objavo – accepted for publication: 2025-01-13

doi:10.17222/mit.2024.1344

The long-distance oil pipeline in the R-K region of Chad has experienced frequent failures of heat-shrink sleeves, significantly impacting normal production in the oilfield. Therefore, a systematic study of the soil corrosion behaviour of pipelines after heat-shrink sleeve damage is essential before implementing targeted anti-corrosion measures to prevent and control soil corrosion. Through sample composition analysis, electrochemical testing, and immersion experiments on the crude oil pipeline in the specified area of Chad, as well as morphology and composition analysis of the corrosion products formed on the pipeline, the main cause of corrosion failure was inferred to be the high content of CO_2 and Cl? in the soil, as their synergistic effect induces pitting corrosion on the pipeline. Furthermore, the high humidity and abundant rainfall in the Chad region increase the corrosion risk. The primary soil corrosion products are Fe_2O_3 and $FeCO_3$, along with small amounts of Fe_3O_4, FeCl (OH), and $CaCO_3$. The average corrosion rate along the pipeline soil line ranges from 0.10 to 0.13 mm a^{-1}.

Keywords: soil corrosion, CO_2, corrosion mechanism, corrosivity model

Na zelo dolgih naftovodih, kot je naprimer R-K naftovod (od začetne postaje črpanja Ronier do končne postaje Kome) v afriškem Čadu, pogosto odpovejo polietilenski zaščitni toplotno skrčljivi rokavi (angl.: heat shrink sleeves), kar pomembno vpliva na normalno proizvodnjo oziroma črpanje nafte na naftnih poljih. Zato so se avtorji tega članka odločili za sistematično študijo korozije povzročene z zemljino oziroma okolico, ki jih obdaja po tem, ko je že prišlo do poškodbe toplotno skrčljivega rokava. V tem primeru je bilo v študiji treba uporabiti pomembne ciljane antikorozijske ukrepe, ki preprečujejo korozijo povzročeno z okoliško zemljino oziroma okolico. Avtorji so tako izvedli vzorčenje in analizo sestave, elektrokemijsko testiranje in preizkuse potapljanja na surovih (nezaščitenih) vzorcih naftovodov v specifičnem okolju, ki se nahaja v Čadu. Prav tako so naredili morfološko in kemijsko analizo korozijskih produktov na naftovodih. Avtorji glavni razlog za korozijske poškodbe pripisujejo visoki vsebnosti CO_2 in Cl_2 v zemljini oziroma okolici, katerih sinergijski učinek je inducirana luknjičasta (točkasta) korozija (angl.: pitting corrosion) na naftovodih. Nadalje visoka vlažnost in obilna deževja v tem analiziranem področju Čada povečujejo nevarnost za korozijske poškodbe. Osnovni nastali korozijski produkti so Fe_2O_3 in $FeCO_3$. Poleg tega so avtorji našli tudi manjše vsebnosti Fe_3O_4, FeCl(OH) in $CaCO_3$. Povprečna ugotovljena hitrost korozije zaradi navedenih okoljskih vplivov vzdolž naftovoda je bila od 0,10 do 0,13 mm na leto.

Ključne besede: zemeljska korozija, CO_2, korozijski mehanizem, korozijski model

1 INTRODUCTION

Long-distance crude oil pipelines frequently encounter severe corrosion challenges during transportation. To mitigate the corrosion rate, polyethene heat-shrinkable sleeves are employed to insulate these pipelines from corrosive media during installation. In Chad, the rainy season is characterized by high precipitation, with local soil moisture content often exceeding 50 %. This results in long-distance crude oil pipelines being continuously submerged in high-temperature, water-saturated soils. The efficacy of heat-shrinkable sleeves under such conditions hinges on their ability to reduce water absorption, which at elevated temperatures can decrease viscosity and consequently lead to pipeline detachment. This detachment facilitates the exposure of the pipeline to the corrosive medium, thereby initiating the corrosion process. For natural gas pipelines, the deployment of polyethene heat-shrinkable sleeves is a common practice due to their advanced development and suitability for filling material gaps. However, the sleeves used as the filler of pipeline ring welds often exhibit defects such as warping, peeling, and breakage, compromising their integrity.[1] The primary failure modes of in-service pipeline

*Corresponding author's e-mail:
jc_liuchengl@cnpc.com.cn (Chenglei Liu)

heat-shrinkable sleeve patching include warping, folding, carbonization, and bubbling, with the last one being the most significant factor affecting the quality of the patching.[2] Research indicates that the predominant form of failure in the application of pipeline heat-shrinkable sleeve patching is the loss of interface sealing performance. Furthermore, damage or removal of the anti-corrosion layer may lead to cathodic protection current shielding issues, thereby diminishing the effectiveness of cathodic protection. The failures of heat-shrinkable tapes can be attributed to two primary factors: firstly, the performance of the heat-shrinkable tape and ancillary products fails to meet the stringent requirements of the anti-corrosion patching process; secondly, the environmental conditions at the site and the quality control during the construction process are not sufficiently rigorous.

It is imperative to undertake a systematic investigation into the corrosion behaviour of soil surrounding pipeline joints after a heat-shrinkable sleeve has ruptured. This study aims to facilitate the implementation of effective anti-corrosion measures for pipelines, thereby preventing and controlling the onset of corrosion. Pipeline corrosion can be categorized into two primary forms: uniform corrosion and localized corrosion. Localized corrosion, which is particularly susceptible to the formation of corrosion pits, poses a significant threat to the safety of oil fields.[3] In comparison, uniform corrosion affects the entire pipeline and its rate can be readily measured and predicted.[4] A substantial body of research has been dedicated to investigating the correlation between soil composition and the rate of metal pipeline corrosion. Understanding these dynamics is crucial for developing more effective corrosion prevention strategies and enhancing the longevity and safety of pipeline infrastructure.

Xie[5] utilized a polarization test method to demonstrate that the corrosion rate of metals increases with increasing chloride ion (Cl^-) concentration. Conversely, other scholars argue that this phenomenon can be attributed to the ability of Cl^- to disrupt the passivity of steel, thereby inducing pitting corrosion. Xie conducted an orthogonal test involving sand containing Cl^-, sulphate (SO_4^{2-}), and bicarbonate (HCO_3^-) ions, concluding that SO_4^{2-} exerts a greater influence on the electrochemical corrosion behaviour of the sand when these three anions coexist.[6] Dehwah et al. explored the impact of a simultaneous presence of sulphate and chloride on the corrosion of steel bars, finding that an increase in the sulphate concentration intensifies the chloride-induced corrosion of steel bars.[7] Roland examined the effects of SO_4^{2-} and Cl^- on the local corrosion performance and morphology of 409 ferritic stainless steel, finding that the corrosion rate of SS409 is directly proportional to the concentration of these anions in the electrolyte.[8] In a related investigation, Katsuhiko et al. observed that Cl^- deposition is likely at locations with thin rust layers on carbon steel surfaces, leading to a looser and more porous rust layer structure.[9] This alteration allows external Cl^- to penetrate and accelerate corrosion. However, over an extended observation period, as the rust layer on the carbon steel surface thickens, the corrosive impact of external Cl^- diminishes, and the formation of chloride slows down.[10]

The climatic conditions in Chad have a significant impact on pipeline corrosion, as the country spans from the arid environment of the Sahara Desert to the high-humidity regions of the southern tropical savannas. High humidity and abundant precipitation increase the risk of pipeline corrosion.[11] The moisture and dissolved salts in the soil can promote electrochemical corrosion, particularly at points of pipeline damage or coating failure. However, there has been limited research on the soil corrosion behaviour of oilfield pipelines in the Chad region.

Therefore, this article focuses on the external corrosive media affecting X65 oilfield pipelines in the Chad area, conducting an in-depth mechanistic analysis. Based on this analysis, a comprehensive data model is established to assess the soil corrosivity in the Chad region, which can contribute to the study of soil corrosion behaviour in different areas. Field data collection and relevant testing are conducted on the Phase II pipeline in Chad (from the Ronier Launch Station to the Kome End Station), integrating and analysing fundamental information and external inspection data to identify the causes and growth trends of defects. Additionally, the effectiveness of cathodic protection for the pipeline is tested and evaluated. The soil along the pipeline, excavated corrosion products, and the transported media are sampled and analysed for composition. Electrochemical methods and embedded coupon techniques are employed to study the corrosion mechanisms and influencing factors of the pipeline.[12] Finally, based on the research findings and combined with the actual operational environment and transmission conditions of the pipeline, research on predictive technologies for pipelines is carried out, leading to the development of a mechanistic model of soil corrosion and a model for evaluating soil corrosivity.

2 EXPERIMENTAL PART

The study focuses on the Φ508 Chad Phase II crude oil pipeline (from the Ronier Launch Station to the Kome End Station) under the jurisdiction of China National Petroleum Corporation International (Chad). The pipeline has a total length of 196 km, a diameter of 508 mm, and it transports crude oil. It is made of API 5L X65 material, with wall thicknesses of 7.9 mm and 11.1 mm, a design pressure of 10 MPa, and a 3PE anti-corrosion coating.

2.1 Soil sample testing

Soil sample testing methods included the hand rubbing method, dried residue weight method, and spectrophotometry, following the standard GB/T 39637-2020 Corrosion of Metals and Alloys – Classification of Soil

Corrosivity. A comprehensive evaluation of soil corrosivity was conducted, as shown in **Table 1**.

Soil samples were taken along the pipeline route (from the Ronier Launch Station to the Kome End Station) at intervals of 4 km, yielding a total of eight soil samples designated as 1#, 2#, 3#, 4#, 5#, 6#, 7# and 8#.

Table 1: Soil sample testing methods and standards

Serial number	Test parameter	Test method	Evaluation criteria
1	Soil texture	Hand rubbing method	GB/T 396370-2020 Corrosion of Metals and Alloys – Classification of Soil Corrosivity
2	Moisture content	Dry residue weighing method	
3	Cl^- and SO_4^{2-}	Spectrophotometric method	
4	Total salinity	Drying method	
5	pH value	Potentiometric method	
6	Redox potential	Depolarization method	

In conjunction with the actual conditions of the Chad Phase II oil pipeline, key parameters such as soil texture, moisture content, Cl^- content, SO_4^{2-} content, total salt content, pH value, and redox potential were tested on the eight soil samples. Additionally, the electrochemical behaviour and corrosion effects of X65 steel in the soil samples were observed, ultimately assessing the soil corrosivity of X65 steel.[13,14]

2.2 Electrochemical testing

Standard X65 corrosion test coupons were cut into test samples with dimensions of (10 × 10 × 2) mm using a CNC spark erosion cutting machine. Copper wires were connected to the backside of the processed sample working surface using a conductive adhesive, and the remaining parts were sealed with epoxy resin. After drying for 24 h and polishing with a metallographic polishing machine, the samples were prepared as working electrodes.[15]

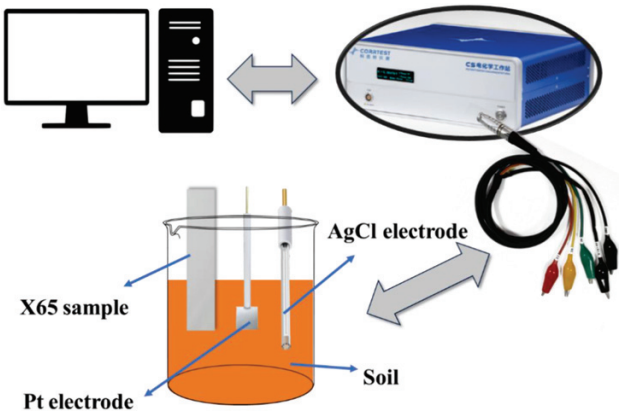

Figure 1: Electrochemical testing of x65 steel in soil samples

The electrochemical performance of X65 steel in soil samples was tested using a CS310M electrochemical workstation (Wuhan Coster Instrument). As shown in **Figure 1**, in the three-electrode system, a saturated silver chloride electrode served as the reference electrode, a platinum electrode as the auxiliary electrode, and the electrolytes were soil samples from different regions (1#, 2#, 3#, 4#, 5#, 6#, 7#, 8#). The X65 steel was used as the working electrode to conduct the corresponding electrochemical tests (with adjustments made for water content).[16]

Electrochemical tests included open-circuit potential (OCP), electrochemical impedance spectroscopy (EIS), and potentiodynamic Tafel scan. Before electrochemical testing, it was necessary to ensure that the samples had reached a steady state in the corrosive medium. The open-circuit potential and electrochemical impedance of the samples were first measured, followed by the determination of the self-corrosion potential and time curve (E_{corr} – t curve), as well as linear polarization and potentiodynamic polarization curves. The EIS testing frequency range was 10^{-2} to 10^5 Hz, with an AC amplitude of 10 mV. The potentiodynamic scan range was –0.1 to +0.4 V, with a scanning rate of 0.5 mV s^{-1}, and all potentials were referenced to the saturated silver chloride solution. Impedance analysis and equivalent circuit fitting of the impedance spectrum curves were performed using ZView2 software. Tafel fitting of the polarization curves was carried out using Cview2 software, with the fitting region being the approximately linear region that is 50–100 mV away from the self-corrosion potential.[17]

2.3 Buried plate method

Buried weight loss experiments were conducted to study the corrosion effects of eight different soil samples on X65 steel. Each soil sample was precisely weighed to 1000 g using an electronic balance, and any debris was removed to ensure the purity and consistency of the samples. Following the ISO 11277-2020 standard, the soil samples were ground and sieved to approximately 250 mesh size. The processed soil was placed into transparent boxes with dimensions of (100 × 120 × 230) mm. Standard X65 corrosion coupons, with dimensions of (75 × 25 × 5) mm, were first cleaned with distilled water, then with anhydrous ethanol, dried, and uniformly buried in different soil samples.[18]

The experiment was designed to include three different cycles: 15 d, 25 d, and 35 d. At the end of each experimental cycle, the coupons were retrieved from the soil, subjected to acid and alkaline washing, and then cleaned with deionized water and soft brushes to remove soil residues and corrosion products. They were then cleaned with ethanol and air-dried. After cleaning, each coupon was weighed, the weight changes were recorded, and corrosion rates were calculated based on the weight loss and periods. After integrating all experimental data, corrosion weight loss curves were plotted based on the

Table 2: Soil sample testing results

Soil number	Soil texture	Moisture content (%)	pH	Salinity (mg g^{-1})	Cl^- (mg g^{-1})	SO_4^{2-} (mg g^{-1})	CO_3^{2-} (mg g^{-1})	HCO_3^- (mg g^{-1})	Redox potential (mV, SHE)	Natural corrosion potential (mV)
1#	Coarse loam	50	6.5	0.568	0.031	0.326	0.124	0.267	176	-442
2#	Clay	50	5.8	0.984	0.077	0.357	0.254	0.847	153	-374
3#	Sandy soil	50	6.8	0.712	0.048	0.137	0.420	0.354	155	-445
4#	Medium loam	50	6.5	1.633	0.034	0.246	0.573	0.744	201	-347
5#	Coarse loam	50	6.1	0.875	0.130	0.148	0.247	0.895	167	-364
6#	Sandy soil	50	7.1	2.016	0.053	0.403	0.114	0.247	145	-474
7#	Coarse loam	50	6.5	1.245	0.056	0.189	0.254	0.528	142	-465
8#	Light clay	50	6.3	5.526	0.133	1.019	0.942	1.452	208	-548

corrosion weight loss data to demonstrate the corrosion rates of steel under different soil conditions[19]. The calculation formula is as follows:

$$v = \frac{\omega_0 - \omega_1}{s \cdot t} \quad (1)$$

In the Equation (1) v – the corrosion rate of the metal, g m^{-2} h^{-1}; ω_0 – the weight of the specimen before corrosion, g; ω_1 – the weight of the metal after corrosion and the removal of corrosion products, g; s – the surface area of the specimen exposed to the corrosive medium, m^2; t – the time of the specimen's corrosion, h.

$$v_l = 8.76 \times \frac{v}{\rho} \quad (2)$$

In the Equation (2) v_l – the corrosion rate expressed by corrosion depth, mm a^{-1}, ρ – the density of the metal, g cm^{-3}.

Based on the corrosion rate of X65 steel in different soil samples, the annual corrosion rate was inferred, thereby providing a direct understanding of the corrosiveness of different soil samples towards X65 steel.

2.4 Morphology and analysis of corrosion products

The samples were cut to dimensions of (10 × 10 × 3) mm using an electro spark CNC cutting machine. Before testing, the upper and lower surfaces of the samples were abraded with 400- and 800-grit sandpapers, respectively, and then cleaned using an XRD-6000 ultrasonic cleaner. The scanning range of the instrument was set to 20–90°, with a scanning speed of 4° min^{-1} and a step size of 0.02°. The data acquired from the test were analysed using Jade 5 software. The samples were observed under a Hitachi S-3400N scanning electron microscope (SEM), with the analysis of microcomponents performed using an energy-dispersive spectrometer (EDS).

3 RESULTS AND DISCUSSION

3.1 Soil sample testing results

Before testing, it was found that the moisture content of the eight soil samples collected for this study was low, suggesting that excessive evaporation and loss of moisture had occurred due to prolonged collection and storage times. Through the analysis of the natural environment along the Chad Phase II pipeline, it was determined that the average rainfall during the rainy season for this region can reach up to 900–1400 mm. According to the relevant soil moisture datasets/soil water content datasets (2000–2020), the soil moisture content can reach 40–60 %.

Considering the aforementioned factors, and in conjunction with the hydrological data obtained along the pipeline as well as geological exploration data, the soil moisture content during the Chad rainy season is assumed to be 50 %.[20] Water was added to the soil samples collected in this study to adjust the moisture content to 50 %, and the relevant tests were conducted again. The test results are shown in **Table 2**.

At a moisture content of 50 %, the redox potential was lower compared to when the moisture content was lower, indicating a decrease in soil oxidisability; the natural corrosion potential increased – the more positive the natural potential of the soil, the lower its corrosivity. In other words, an increase in the moisture content generally reduces soil corrosivity.

In light of the actual operating environment of the Chad Phase II pipeline, it is inferred that the continuous rainy season is not the stage, in which pipeline corrosion is most severe. The alternation between dry and rainy seasons, leading to fluctuating wet and dry states, actually exacerbates the occurrence and progression of corrosion.

3.2 Electrochemical test results

Typically, electrochemical behaviour and reaction rates are characterized using impedance spectroscopy and polarization curves,[21] where impedance spectroscopy represents the interface resistance or capacitance between the electrode and the electrolyte, while polarization curves describe the polarization behaviour of the electrode in the electrochemical system using corrosion current density as a key parameter and evaluate the corrosion performance and corrosion resistance of a material.[22]

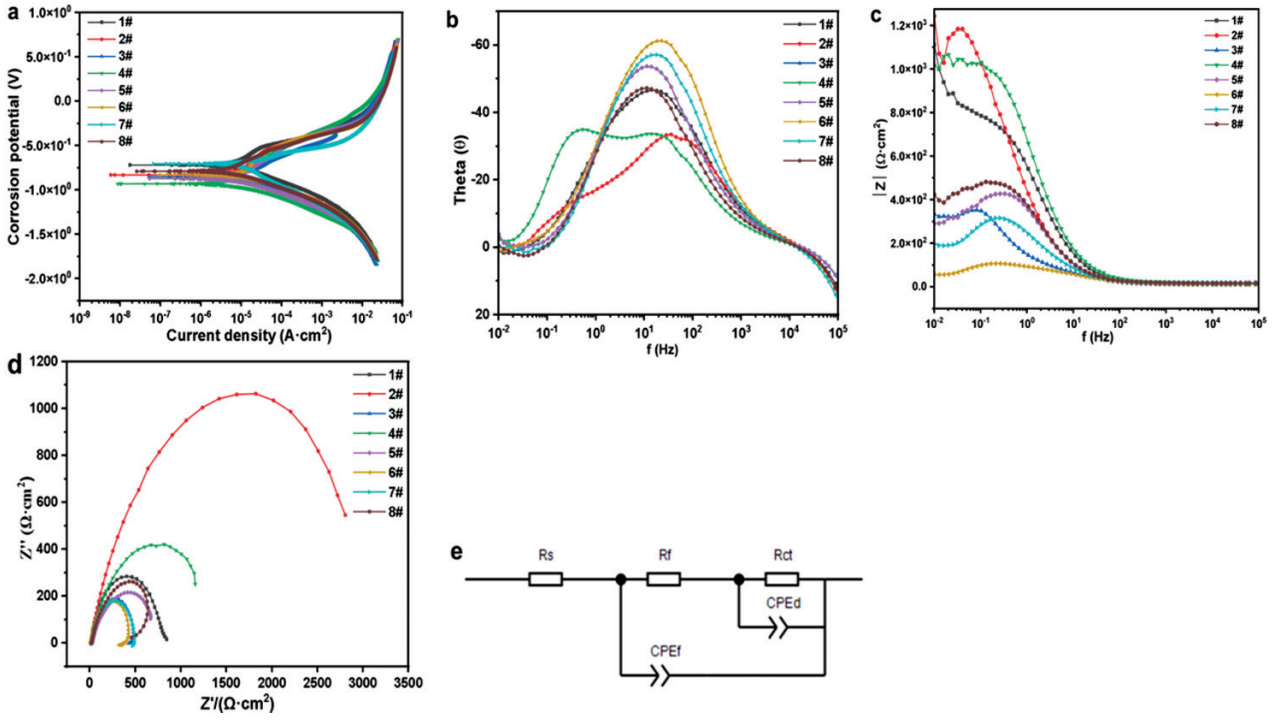

Figure 2: Electrochemical test results: a) polarization curve; b) Bode plot; c) phase angle plot; d) impedance spectrum; e) impedance fitting circuit diagram

The polarization curves, Nyquist plots, Bode diagrams, and phase angle plots of eight soil samples are shown in **Figures 2a** to **2d**. According to the corrosion current density in the polarization curves, X65 steel exhibits a higher corrosion current density in soil samples 3#, 6#, and 7#. The increase in the corrosion current density indicates a stronger tendency for self-corrosion and a faster anode reaction rate. In the phase angle plots, it can be observed that most soil samples display a single peak, while soil sample 4# presents two peaks. The number of peaks is closely related to the number of capacitive loops in the Nyquist plots. In the Bode diagrams, the trend of

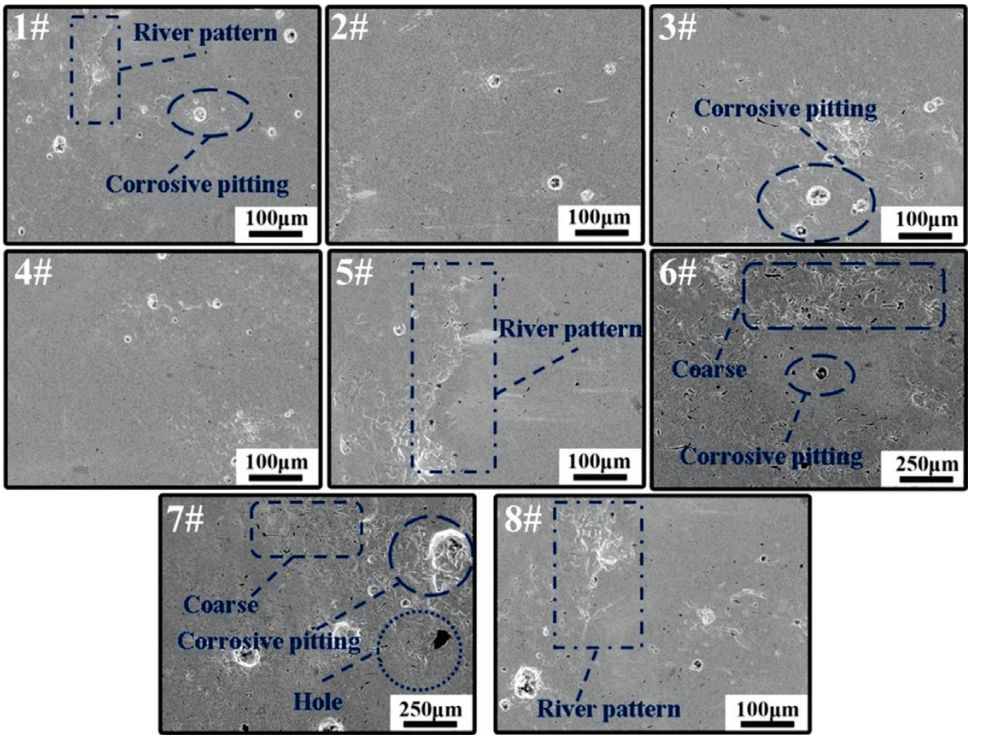

Figure 3: Microscopic corrosion morphology of X65 steel surface after electrochemical testing

|Z| values corresponds with the radius of the capacitive loops, following the order of 2# > 4# > 1# > 8# > 5# > 3# > 7# > 6#, with the |Z| value of soil sample 2# being the highest, 0.01 Hz. In the Nyquist plots, a smaller capacitive arc indicates a faster charge transfer rate, suggesting a more intense corrosion reaction. Soil sample 6# has the smallest capacitive arc, indicating the most severe corrosion reaction, which is consistent with the results obtained from the soil sample testing and analysis.

The equivalent circuit diagram obtained by fitting the EIS data with Zview2 software is shown in **Figure 2e**, where R_s is the solution resistance, R_{ct} is the charge transfer resistance, CPE_d is the constant phase element representing the double layer capacitance, R_f is the resistance of the corrosion product film, and CPE_f is the constant phase element representing the capacitance of the corrosion product film.

Figure 3 depicts the microscopic corrosion morphology of the X65 steel electrode after electrochemical testing. Following electrochemical testing, the sample surface experienced pitting and crevice corrosion, resulting in a distribution of small or large irregular corrosion products on the surface of the electrodes, along with numerous protrusions and micro-pits. The corrosion surfaces of the 3#, 6# and 7# samples showed severe pitting, with a rougher surface texture and the presence of some larger holes and black substances. This was due to their soil being sandy or light loamy, with high Cl^- concentrations and relatively high natural corrosion potentials. In the electron microscopy images of the 1#, 5# and 8# samples, river-like undulations can be observed, which are indicative of groove corrosion. This was caused by cracks and deposits on the electrode surface, as well as possibly the paths formed by the flow of corrosion products over the electrode surface. The fewer corrosion products in these samples are attributed to their lower salinity, natural corrosion potentials and pH values. In the electron microscopy images of the 2# and 4# samples, a smooth and flat surface can be seen, with few and small crevice holes, indicating very minor corrosion. This is closely related to the soil type and ion concentrations of these samples.

3.3 Immersion test results

The soil physical and chemical properties, as well as the average corrosion rates of X65 steel in the soil samples (1#,2#,3#,4#,5#,6#,7# and 8#) under conditions of 50 % moisture content, are shown in **Figure 4**. The test revealed that the average corrosion rates of the eight soil samples were relatively close, ranging between 0.10–0.13 mm a^{-1}. The highest corrosion rate was observed for the 6# soil, 0.133 mm a^{-1}, while the lowest was observed for the 2# soil, 0.104 mm a^{-1}. The differences in the corrosion rates may be attributed to variations in the soil texture and significantly different natural corrosion potentials. It should be noted that with the buried plate (weight loss) method, the primary form of metal corrosion is uniform corrosion, with a relatively uniform electrochemical activity between the entire metal surface and the soil environment. Metal loss occurs in a relatively uniform manner over the entire metal surface, without any distinct independent or selective corrosion regions.

The primary form of corrosion encountered in the second phase of the crude oil pipeline in Chad is external corrosion, particularly at patch-up areas. This corrosion is typically manifested as a combination of localized and, to a lesser extent, uniform corrosion.[23] Unlike uniform corrosion, which occurs evenly across a metal surface, localized corrosion, including pitting, is concentrated in specific areas. This type of corrosion is often driven by the heterogeneity of the soil's microenvironment, which can vary significantly in terms of pH, ion concentration, and oxygen availability.[24] Specifically, factors such as gradients in redox potential, localized increases in chloride ion (Cl^-) concentrations, and decreases in pH can intensify corrosion rates in certain regions of the pipeline.[25]

Building on previous research, it was established that the predominant form of corrosion in the second phase of the crude oil pipeline in Chad is external corrosion at patch-up areas. The observed corrosion morphologies include: 1) extensive continuous pit corrosion and 2) clusters of adjacent corrosion pits. These findings indicate a combination of localized and, to some extent, uniform corrosion. The onset of external corrosion in these areas is primarily attributed to weakened bonding at lap joints, which permits the ingress of free water. This creates a distinct microenvironment conducive to corrosion, characterized by variations in the composition of corrosive media and more aggressive local corrosion dynamics compared to generalized soil corrosion. Notably, the rate of localized corrosion in these areas typically exceeds that measured by the traditional buried plate (weight loss) method.

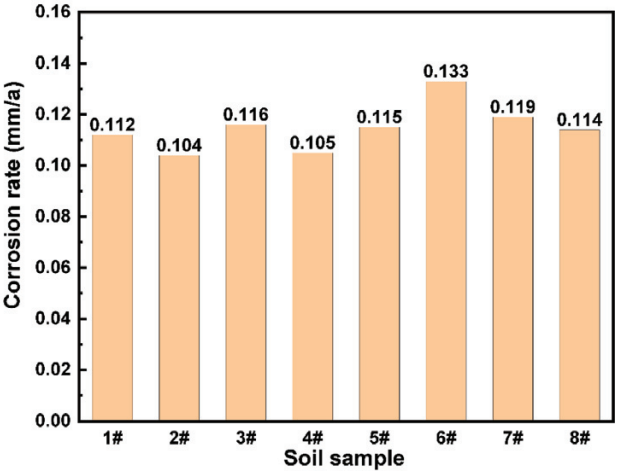

Figure 4: Annual corrosion rate curves and average annual corrosion rate curves of X65 steel under 50 % moisture content

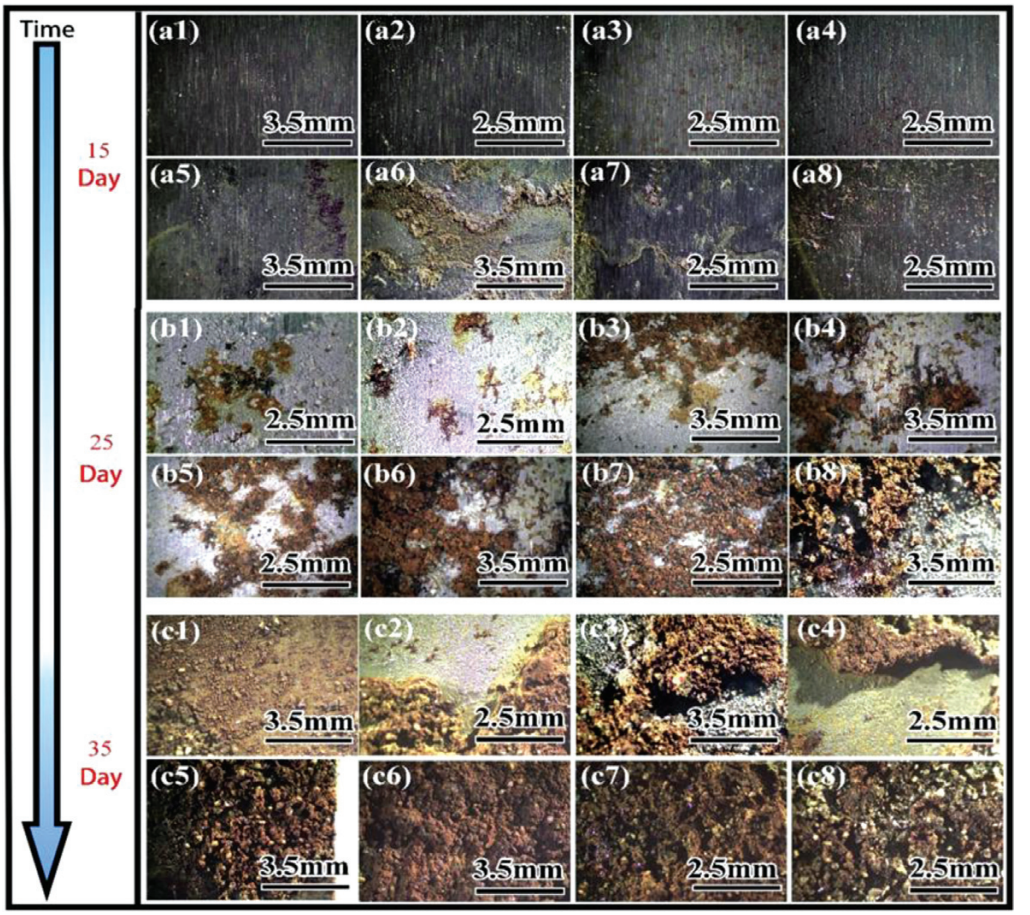

Figure 5: Macroscopic corrosion morphology of X65 steel surface under different soil moisture contents: a) day 15; b) day 25; c) day 35

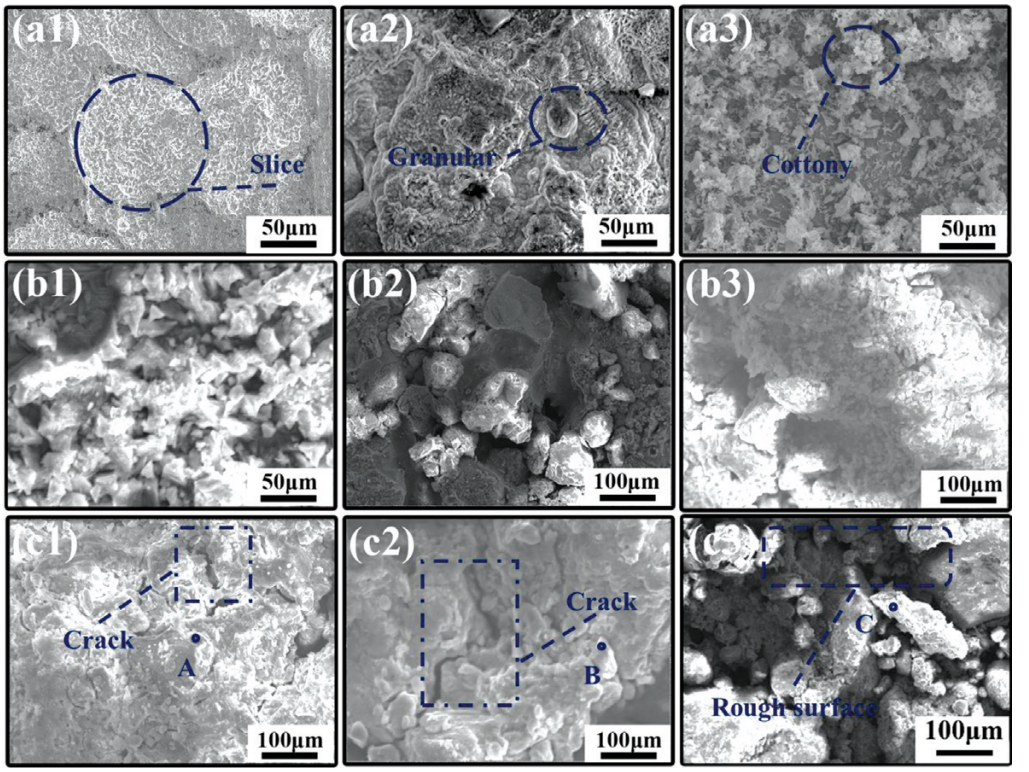

Figure 6: Microscopic corrosion morphology of X65 steel surface at 50 % soil moisture content: a) day 15; b) day 25; c) day 35

For this study, a point of significant metal loss was identified and excavated from each soil sample. Corrosion products on the external surface of X65 steel were then collected and analysed microscopically, as depicted in **Figure 5**. Initial observations after 15 d revealed minimal corrosion on most of the X65 steel samples, maintaining clear surface textures. Notably, only isolated corrosion products were visible on the steel from soil 6#. By day 25, a uniform and continuous layer of corrosion products formed across the steel surfaces, though the coverage was somewhat sparser at the edges. This pattern aligns with the findings from our electrochemical experiments. By day 35, the film of corrosion products began to break down, leading to intensified corrosion characterized by numerous reddish-brown corrosion products.

In an investigation of X65 steel exposed to eight different soil samples with varying moisture contents, it was observed that the steel's original metallic lustre was obscured by a reddish-brown ferric oxide film, a by-product of the oxidation process. Microscopically, this film displayed consistent roughness and patchy distribution. Over time, the oxidation led to the formation of an amorphous, protective rust layer on the steel's surface, which engaged in slow interfacial reactions with the underlying metal. Microscopic analysis further revealed a stratified structure within the rust layer, suggesting complex formation dynamics. The compactness of the rust layer, indicative of its strong adherence to the substrate, highlights a distinct mechanism of rust layer development in the context of soil-induced corrosion. Notably, while this uniform corrosion did not produce through-holes or severe material degradation, the integrity of the rust film significantly modified the physical properties of the metal surface.

Macroscopic analysis indicated that the corrosion patterns of samples 1#, 2#, and 4# displayed notable similarities, as did the patterns observed in samples 3#, 5#, and 8#, and samples 6# and 7#. Based on these groupings, the most severely corroded regions of samples 1#, 3#, and 6# were selected for further analysis at specific intervals: (15, 25, and 35) d, respectively. These regions were examined using scanning electron microscopy (SEM) to elucidate the detailed corrosion mechanisms and morphological changes. The results of this SEM analysis are presented in **Figure 6**.

The analysis of the corrosion products on X65 steel samples exposed to soil environments revealed distinct morphological differences: in sample a1, the products formed sheet-like structures; in a2, they were granular; and in a3, they appeared more dispersed. With an increased exposure time of 25 d, the corrosion products in sample b1 became more dispersed and exhibited significant variations in height. In samples b2 and b3, the products transitioned from smaller to larger grains, accumulating into thicker layers. After 35 d, all sample groups (c1, c2, and c3) developed thick, sheet-like corrosion layers, characterized by noticeable porosity and cracking, which underscored the aggressive interaction between the corrosion medium and steel.[26] The surface of these layers was coated with dense iron oxide particles, resembling sand grains, and hydroxides with a flocculent structure, indicative of ongoing oxidation and hydration reactions. Further microscopic examination revealed the presence of white, flower-like or network-like structures, which were loosely arranged and porous hallmarks of immature hydrated iron oxides. The formation of a dense compound layer, identified as hydroxide iron oxide ($FeO_x{\cdot}(OH)_{3-2x}$), potentially serves as a protective barrier against further oxidation of the steel surface.

The base composition of X65 steel primarily includes carbon (C), manganese (Mn), and iron (Fe). Analysis of the corrosion products, however, reveals a different elemental composition, dominated by carbon (C) and oxygen (O), suggesting a predominant formation of iron oxides (Fe_2O_3) and iron carbonates ($FeCO_3$). This indicates an active participation of carbon dioxide (CO_2) in the corrosion process. Additionally, minor constituents such as iron(II, III) oxide (Fe_3O_4), iron chloride hydroxide (FeCl(OH)), and calcium carbonate ($CaCO_3$) were detected, highlighting the involvement of oxygen (O_2), chloride ions (Cl^-), and carbon dioxide (CO_2) in the corrosion dynamics. Energy-dispersive spectroscopy (EDS) was performed on selected points within the most severely corroded regions of samples 1#, 3#, and 6# after 35 days of exposure[27]. The results of this analysis are presented in **Figure 7**.

The results of the energy-dispersive X-ray spectroscopy (EDS) revealed that the predominant elements in

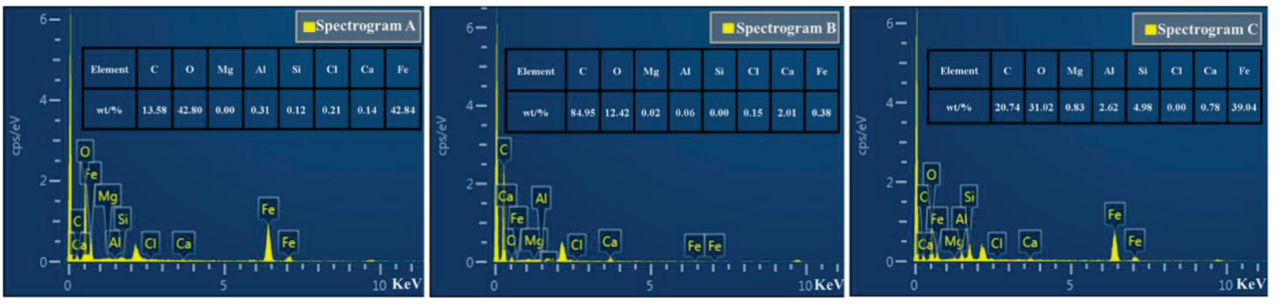

Figure 7: Elemental analysis spectrum of corroded surface of X65 steel

the corrosion zone are carbon (C), oxygen (O), and iron (Fe), with minor traces of aluminium (Al), silicon (Si), and calcium (Ca) detected in localized microzones. These trace elements are likely to influence the corrosion process significantly. As depicted in **Figure 7**, the elemental analysis of the corrosion surface presents varied compositions: Spectrum A shows a higher concentration of iron (Fe) and oxygen (O), indicating that the corrosion products predominantly consist of iron oxides. In Spectrum B, elevated levels of carbon (C) and oxygen (O), along with lower concentrations of calcium (Ca) and iron (Fe), suggest that the surface corrosion products are primarily composed of carbon oxides and carbonates. Spectrum C reveals a higher concentration of carbon (C), oxygen (O), and iron (Fe), with trace amounts of magnesium (Mg), aluminium (Al), and silicon (Si), indicating a composition of carbonates and iron oxides in the corrosion products.

In the 35-day buried-plate experiment, corrosion products were collected from the more severely corroded regions of the X65 steel in samples 1#, 3#, and 6# for phase analysis using an X-ray diffractometer, as depicted in **Figure 8**. The analysis revealed that the primary constituents of the corrosion products in sample 1# are siderite ($FeCO_3$) and hematite (Fe_2O_3), with minor traces of magnetite (Fe_3O_4) and iron chloride hydroxide (FeCl (OH)). In sample 3#, the dominant components are hematite (Fe_2O_3), calcite ($CaCO_3$), and siderite ($FeCO_3$), supplemented by trace amounts of magnetite (Fe_3O_4) and iron chloride hydroxide (FeCl (OH)). Similarly, the main components in sample 6# are siderite ($FeCO_3$) and hematite (Fe_2O_3), with trace amounts of magnetite (Fe_3O_4) and iron chloride hydroxide (FeCl (OH)). These findings corroborate the results obtained with the EDS analysis and align with the composition of corrosion products collected from the field, further confirming that the white deposits identified in the microanalysis are iron hydroxides.[28] This consistency supports the conclusion that the corrosion of X65 steel in Chad's soil is predominantly due to iron oxidation.

Through experimental research and theoretical analysis of the factors influencing the corrosion of oil field pipelines, the identified corrosion mechanism involves the external environment of the gathering and transportation pipelines, which constitutes a coexisting system of CO_2, Cl^-, and H2O. Utilizing EDS line scanning and XRD phase analysis, it has been determined that the primary corrosion products are siderite ($FeCO_3$) and hematite (Fe_2O_3), with minor traces of magnetite (Fe_3O_4), iron chloride hydroxide (FeCl (OH)), and calcite ($CaCO_3$). The corrosion of X65 steel primarily occurs through three processes: chemical reactions at the gas-liquid interface, within the soil, and the soil/steel interface; charge transfer at the soil/steel interface; and the mass transfer of corrosive substances through the soil. The dissolution of CO_2 gas into water results in the formation of

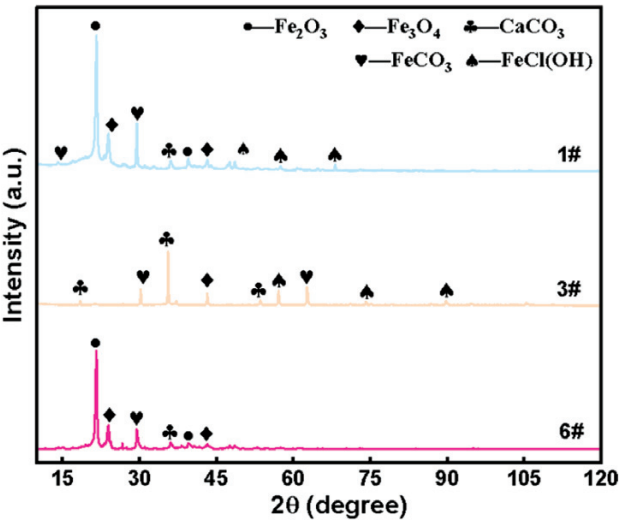

Figure 8: XRD pattern of soil corrosion products on X65 steel pipelines

carbonic acid (H_2CO_3), represented by the following chemical Equations:

$$CO_2 \rightarrow CO_{2\ (aq)} \quad (3)$$

$$CO_{2(aq)} + H_2O \rightarrow H_2CO_3 \quad (4)$$

$$H_2CO_3 \rightarrow H^+ + H_2CO_3 \quad (5)$$

$$HCO_3^- \rightarrow H^+ + CO_3^{2-} \quad (6)$$

The reactions in the soil include 1 anodic reaction and 3 cathodic reactions.

$$Fe \rightarrow Fe^{2+} + 2e^- \quad (7)$$

$$H^+ + e^- \rightarrow H \quad (8)$$

$$H_2CO_3 + e^- \rightarrow H + HCO_3^- \quad (9)$$

$$HCO_3^- + e^- \rightarrow H + CO_3^{2-} \quad (10)$$

The reaction of $FeCO_3$ and $CaCO_3$ deposition on the surface of X65 pipelines.

$$Fe^{2+} + CO_3^{2-} \rightarrow FeCO_3 \quad (11)$$

$$Ca^{2+} + CO3^{2-} \rightarrow CaCO_3 \quad (12)$$

$$FeCO_3 \rightarrow FeO + CO_2 \quad (13)$$

$$3FeO + H_2O \rightarrow Fe_3O_4 + H_2 \quad (14)$$

Due to the anion selectivity of CO2 and the presence of defects in the corrosion product film, chloride ions (Cl-) come into contact with the X65 steel pipeline, thereby promoting pitting corrosion.

$$Fe{+}Cl^- + H_2O \rightarrow [FeCl(OH)]_{ad}^- + H^+ + e^- \quad (15)$$

$$[FeCl(OH)]_{ad}^- \rightarrow FeCl(OH) + e^- \quad (16)$$

Furthermore, the surface of the X65 steel pipeline demonstrates a propensity for pitting corrosion. The in-situ medium contains a high concentration of chloride ions (Cl^-), which continuously accumulate within the pitting holes. Under severe conditions, this accumulation can lead to the perforation of the pipeline.

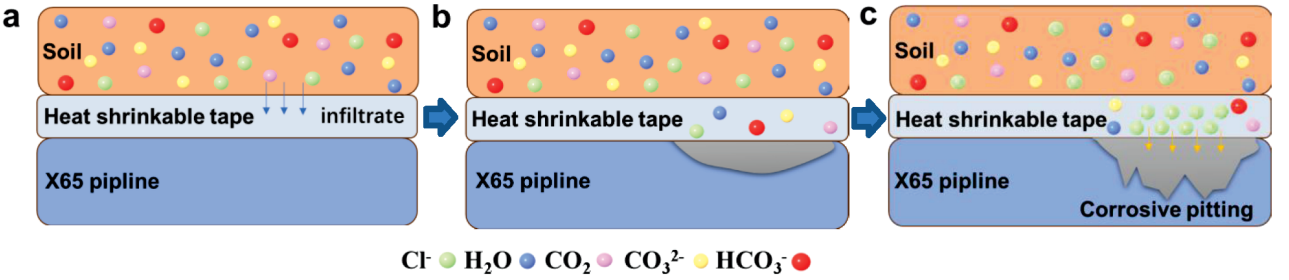

Figure 9: Corrosion mechanism diagram of X65 pipeline closures

3.4 Establishment of a multi-factor soil corrosiveness model

The physicochemical composition of the soil contains more than a dozen elements, which interact and influence each other. The corrosion behaviour of the pipeline is the result of comprehensive interactions of these elements. Therefore, these elements are simplified in this study to achieve an optimal effect, ensuring that the final results can quickly and reasonably evaluate the corrosion environment of the field pipeline.

To simplify the detected elements as much as possible while ensuring the accuracy of the evaluation method, it is first necessary to determine which are the main factors affecting corrosion, and therefore, cluster analysis is first used to mathematically process the relationships between these factors.

The correlation coefficient r_{ij} of various soil physicochemical index data is calculated, with calculation methods including the Euclidean distance method, the maximum-minimum method, the correlation coefficient method, and the scalar product method. In this study, the correlation coefficient method is adopted. The larger the r_{ij}, the stronger the correlation is. The calculation Equation is:[29]

$$r_{ij} = \frac{\sum_{k=1}^{m}(x_{ik} - \bar{x}_i)(x_{ik} - \bar{x}_j)}{\sqrt{\sum_{k=1}^{m}(x_{ik} - \bar{x}_i)^2}\sqrt{\sum_{k=1}^{m}(x_{jk} - \bar{x}_j)^2}} \quad (17)$$

where $\bar{x}_i = \frac{1}{m}\sum_{k=1}^{m} x_{ik}$, $\bar{x}_j = \frac{1}{m}\sum_{k=1}^{m} x_{jk}$.

Based on equations (3)–(15), correlation coefficients for various physicochemical indicators can be calculated, resulting in **Table 4**.

Based on the correlation coefficients of the physicochemical indicators from Table 4, with a standard of 0.70, the above seven physicochemical criteria can be divided into four categories.

Category 1: Water content

Category 2: pH

Category 3: Content of HCO_3^-

Category 4: Content of CO_3^{2-}, content of Cl^-, content of SO_4^{2-}, salt content, and resistivity

The seven physicochemical criteria are considered the main selection parameters for the soil corrosion evaluation. The average annual corrosion rate results were used to perform the calculation using grey correlation analysis[30], and the calculation process was as follows:

$$Y_i = \frac{x_i(k)}{\frac{1}{m}\sum_{k=1}^{m} x_{ik}} \quad i = 1,2,3,\ldots,n;\ k = 1,2,3,\ldots,m \quad (18)$$

where Y_i represents the mean-quantified sequence of each sub-factor, and $X_{i(k)}$ represents the sub-factor series.

$$Y_0 = \frac{x_0(k)}{\frac{1}{m}\sum_{k=1}^{m} x_0(k)} \quad k = 1,2,3,\ldots,m \quad (19)$$

Here, Y_0 denotes the mean-quantified sequence of the parent factors, and $X_{0(k)}$ represents the series of parent factors.

$$f_i = \frac{1}{m}\sum_{k=1}^{m} \xi_i(k) \quad i = 1,2,3,\ldots,n;\ k = 1,2,3,\ldots,m \quad (20)$$

Table 4: Correlation coefficients of various physical and chemical indicators

Index	Moisture content	pH value	CO_3^{2-} content	Cl^- content	SO_4^{2-} content	HCO_3^- content	Salinity	Resistivity content
Moisture content	1.00	–	–	–	–	–	–	–
pH value	–0.45	1.00	–	–	–	–	–	–
CO_3^{2-} content	–0.41	0.48	1.00	–	–	–	–	–
Cl^- content	0.19	0.17	0.50	1.00	–	–	–	–
$htSO_4^{2-}$ content	–0.18	0.30	0.79	0.74	1.00	–	–	–
HCO_3^- content	0.26	0.53	0.48	0.46	0.27	1.00	–	–
Salinity	0.16	0.20	0.55	1.00	0.78	0.46	1.00	–
Resistivity content	0.15	0.20	0.55	1.00	0.80	0.44	0.77	1.00

The grey correlation degrees between each environmental factor and the average corrosion rate, shown in **Table 5**, can be calculated from Equations (3)–(16), (3)–(17) and (3)–(18).

In **Table 5**, it can be observed that the order of influence of each factor on the average corrosion rate of X65 steel is as follows: pH > resistivity > salinity > Cl^- content > CO_3^{2-} content > SO_4^{2-} content > HCO_3^- content.

Subsequently, the weights of various corrosion factors for X65 steel are calculated by establishing a comparison matrix,[31] as shown in **Table 6**.

From **Table 6**, it can be seen that the differences between the weights of the six factors influencing the average corrosion rate of X65 steel are not significant. Moreover, from the calculation results, it is evident that among the four anions (Cl^- content, CO_3^{2-} content, HCO_3^- content, SO_4^{2-} content) of soil corrosion factors, the last three have a very small proportion of influence on the corrosion rate. Considering the feasibility and convenience of on-site operations, only the influence of the Cl-content among the four anions was considered. Correspondingly, the factors such as redox potential, natural corrosion potential, and soil texture were also included as elements for evaluating the corrosivity. The calculation used the same method, and the results are shown in **Table 7**.

Field and laboratory measurements were conducted for various factors such as soil resistivity, moisture content, soil pH, soil texture, redox potential, natural corrosion potential, salinity, and Cl^- content. Each measurement indicator was scored and denoted as N1, N2, ..., N7. The scores for these factors were then summed to obtain the total score N[32]. The soil corrosivity was evaluated based on the N values, with the criteria for the corrosion grade evaluation presented in **Tables 8** and **9**.

Table 5: Grey relational degrees between various environmental factors and the average corrosion rate of X65 steel

Grey relational degree	pH value	CO_3^{2-} content	Cl^- content	SO_4^{2-} content	HCO_3^- content	Salinity	Resistivity content
fi	0.7923	0.7051	0.7078	0.7045	0.6942	0.7230	0.7320

Table 6: Weights of the main factors influencing the soil corrosivity of X65 steel

Index	pH value	CO_3^{2-} content	Cl^- content	SO_4^{2-} content	HCO_3^- content	Salinity	Resistivity content
Weights	0.4479	0.0579	0.0861	0.0467	0.0533	0.1228	0.1853

Table 7: Weights of the main factors affecting soil corrosivity

Indices	Soil texture	pH	Salinity content	Cl^- content	Natural corrosion potential	Soil resistivity	Redox potential
Weights	0.0912	0.2293	0.1197	0.0721	0.1864	0.1673	0.1340

Table 8: Soil corrosivity evaluation indexes

Serial number	Detection indicators	Numerical range	Evaluation scores Ni (i = 1, 2, 3,⋯,7)
1	Soil texture	Sandy soil (strong)	2.5
		Loam (light, medium, heavy)	1.5
		Clay (light clay, clay)	0
2	pH value	4.5–5.5	4
		5.5–9.0	2
3	Salinity (mg g^{-1})	>0.75	3
		0.1–0.75	2
4	Cl^- content (mg g^{-1})	>0.05	1.5
		0.01–0.05	1
5	Natural corrosion potential (mV)	<-550	5
		–550 to –450	3
		–450 to –300	1
6	Soil resistivity (Ω · m)	<20	4.5
		20–50	3
7	Redox potential (mV, SHE)	200–400	1
		>400	0

Table 9: Soil corrosivity classification and evaluation criteria

N value	Soil corrosivity grades
19<N=30	High
11<N=19	Medium

Note: N = N1 + N2 + N3 + N4 + N5 + N6 + N7

Table 10: Evaluation of soil corrosivity in Chad

Number	Soil texture	pH value	Salinity content	Cl^- content	Natural corrosion potential	Soil resistivity	Redox potential	Score
1#	1.5	2	2	1	3	4.5	1	15
2#	0	2	3	1.5	1	4.5	1	13
3#	2.5	2	2	1	5	4.5	1	18
4#	1.5	2	3	1	3	3	0	13.5
5#	1.5	2	3	1.5	3	4.5	1	16.5
6#	2.5	2	3	1.5	5	4.5	1	19.5
7#	1.5	2	3	1.5	5	4.5	1	18.5
8#	0	2	3	1.5	5	4.5	0	16

Based on the detection and evaluation method established above, the corrosivity of X65 steel in the soil of Chad was evaluated, with the results presented in **Table 10**.

Except for the corrosion in soil No. 6, which reached a severe level, the evaluation results of the corrosion of X65 steel in the soil of Chad show that the corrosion of the steel in all other soils was classified as moderate. The average corrosion rates of the eight soils were quite similar, ranging from 0.10 to 0.12 mm a^{-1}. This indicates that the established evaluation system aligns well with the actual evaluation results.

4 CONCLUSIONS

The main conclusions of the soil sample testing, external corrosion product testing, and external corrosion mechanism research are as follows:

1) The soil texture was generally light loam, with a pH value skewed towards neutral, and the overall soil corrosivity was classified as moderate or weak. Among them, soil No. 8 had the highest salinity content, while soil No. 2 had the lowest corrosivity.

2) The corrosion current density was the highest when the steel was in soil No. 6. After impedance fitting, the impedance of soil No. 6 was the smallest, suggesting it had the strongest corrosivity towards X65 steel.

3) The sample surfaces were covered with a reddish-brown iron oxide film. Subsequently, the surface corrosion of the X65 steel after 35 days of indoor corrosion was severe, with the presence of $FeCO_3$, Fe_2O_3 and a small amount of FeOOH on the surface.

4) With an increase in the moisture content (35–55 %), the soil corrosivity towards steel gradually decreased (due to the dilution effect of water on ions and oxygen content), while with an increase in the temperature and Cl^- concentration, the soil corrosivity increased. The average corrosion rate of X65 steel in the eight soil samples with a 50 % moisture content was from 0.10 mm a^{-1} to 0.12 mm a^{-1}.

5) Soil resistivity, moisture content, pH value, soil texture, redox potential, natural corrosion potential, salinity, and Cl^- content are the eight key environmental factors that induce local soil corrosion. The evaluation system aligns well with the actual evaluation results.

5 REFERENCES

[1] L. Kraidi, R. J. Shah, W. Matipa, F. Borthwick, An investigation of mitigating the safety and security risks allied with oil and gas pipeline projects, J. Pipeline Sci. Eng., 1 (**2021**) 3, 349–359, doi:10.1016/j.jpse.2021.08.002

[2] F. Khan, R. Yarveisy, R. Abbassi, Risk-based pipeline integrity management: A road map for the resilient pipelines, J. Pipeline Sci. Eng., 1 (**2021**) 1, 74–87, doi:10.1016/j.jpse.2021.02.001

[3] H. P. Peng, Z. L. Luan, J. Liu, Y. Lei, J. X. Chen, S. Deng, X. P. Su, Corrosion behaviour of X80 pipeline steel in oilfield injection water in Eastern China, Anti-Corros. Methods Mater., 68 (**2021**) 5, 438–448, doi:10.1108/acmm-06-2020-2328

[4] R. Cai, Y. S. Li, S. S. Hao, C. Gao, H. Z. Zhu, P. Wu, Corrosion reason analysis and countermeasures of buried oil unloading pipeline in an oilfield, Eng. Fail. Anal., 163 (**2024**) 14, doi:10.1016/j.engfailanal.2024.108461

[5] Z. B. Wang, Y. G. Zheng, Critical flow velocity phenomenon in erosion-corrosion of pipelines: determination methods, mechanisms and applications, J. Pipeline Sci. Eng., 1 (**2021**) 1, 63–73, doi:10.1016/j.jpse.2021.01.005

[6] J. Zhang, Y. F. Cheng, Modeling of hydrogen atom distribution at corrosion defect on existing pipelines repurposed for hydrogen transport under pressure fluctuations, International Journal of Hydrogen Energy, 58 (**2024**) 1075–1087, doi:10.1016/j.ijhydene.2024.01.213

[7] K. T. Chin, T. Arumugam, S. Karuppanan, M. Ovinis, Failure pressure prediction of pipeline with single corrosion defect using artificial neural network, Oil and Oil Products Pipeline Transportation, 11 (**2021**) 2, 166–171, doi:10.28999/2541-9595-2021-11-2-166-171

[8] G. J. Qin, Y. F. Cheng, A review on defect assessment of pipelines: Principles, numerical solutions, and applications, Int. J. Pressure Vessels Pip., 191 (**2021**) 15, doi:10.1016/j.ijpvp.2021.104329

[9] D. L. Huang, H. Cen, H. Y. Wang, Q. Liu, Z. L. Zong, A. P. Tang, Z. Tang, Study on response patterns and influencing factors of buried pipelines with corrosion defects under fault action, Appl. Eng. Sci., 18 (**2024**) 12, doi:10.1016/j.apples.2024.100176

[10] L. S. Kong, H. B. Li, D. T. Qi, X. M. Li, Z. F. Yan, M. M. Xia, Q. G. Chen, F. S. Wang, X. Fan, Failure analysis of a reinforced thermoplastic pipe used in an oil transportation system, Eng. Fail. Anal., 138 (**2022**) 17, doi:10.1016/j.engfailanal.2022.106403

[11] H. M. H. Farh, M. E. Ben Seghier, T. Zayed, A comprehensive review of corrosion protection and control techniques for metallic pipelines, Eng. Fail. Anal., 143 (**2023**) 22, doi:10.1016/j.engfailanal.2022.106885

[12] M. Nnoka, T. A. Jack, J. Szpunar, Effects of different microstructural parameters on the corrosion and cracking resistance of pipeline steels: A review, Eng. Fail. Anal., 159 (**2024**) 43, doi:10.1016/j.engfailanal.2024.108065

[13] B. Wu, T. T. Yan, L. Chen, H. Z. Wang, Y. Fang, Z. Y. Bao, Electrochemical corrosion behaviour of X80 pipeline steel welded joints fabricated by ultrasound-assisted submerged arc welding in CO2-saturated solution, Int. J. Electrochem. Sci., 19 (**2024**) 3, 10, doi:10.1016/j.ijoes.2024.100475

[14] J. Y. He, F. Xie, D. Wang, G. X. Liu, M. Wu, Y. Qin, Stress corrosion cracking behaviour of buried oil and gas pipeline steel under the coexistence of magnetic field and sulfate-reducing bacteria, Pet. Sci., 21 (**2024**) 2, 1320–1332, doi:10.1016/j.petsci.2023.10.013

[15] F. M. Shimizu, A. M. Pasqualeti, R. M. Carvalho, L. S. Chinelatto, R. A. Fontes, M. H. O. Piazzetta, A. L. Gobbi, R. S. Lima, Combining advanced oxidation principles and electrochemical detection for indirect determination of phosphonate in scale inhibitors employed in the oilfield, Electrochim. Acta, 463 (**2023**) 7, doi:10.1016/j.electacta.2023.142859

[16] R. L. Zhao, B. Wang, D. B. Li, Y. M. Chen, Q. S. Zhang, Effect of sulfate-reducing bacteria from salt scale of water flooding pipeline on corrosion behaviour of X80 steel, Eng. Fail. Anal., 142 (**2022**) 14, doi:10.1016/j.engfailanal.2022.106788

[17] L. Y. Yang, D. L. Zhang, H. M. Fan, Z. W. Tan, S. H. Xing, X. R. Guan, X. Jiang, Investigating the micro-turbulent corrosion mechanism of pipeline defects based on a combined experimental and simulation approach, J. Nat. Gas Sci. Eng., 106 (**2022**) 15, doi:10.1016/j.jngse.2022.104745

[18] J. T. Yuan, L. Tian, W. X. Zhu, S. L. Tan, T. Xin, D. P. Li, W. H. Feng, H. H. Zhang, X. P. Li, J. F. Huang, A. Q. Fu, Y. R. Feng, Internal localized corrosion of X65-grade crude oil pipeline caused by the synergy of deposits and microorganisms, Eng. Fail. Anal., 149 (**2023**) 12, doi:10.1016/j.engfailanal.2023.107276

[19] M. Wasim, M. B. B. Djukic, External corrosion of oil and gas pipelines: A review of failure mechanisms and predictive preventions, J. Nat. Gas Sci. Eng., 100 (**2022**) 22, doi:10.1016/j.jngse.2022.104467

[20] M. C. Elmes, R. M. Petrone, O. Volik, J. S. Price, Changes to the hydrology of a boreal fen following the placement of an access road and below ground pipeline, J. Hydrol.-Reg. Stud., 40 (**2022**) 13, doi:10.1016/j.ejrh.2022.101031

[21] Z. Wang, L. Pang, Y. Zheng, A review on under-deposit corrosion of pipelines in oil and gas fields: Testing methods, corrosion mechanisms and mitigation strategies, Corros. Commun., 7 (**2022**), 70–81, doi:10.1016/j.corcom.2022.03.007

[22] Z. X. Zou, J. Zeng, Z. W. Liu, Y. D. Mo, G. M. Liang, L. L. Wang, Z. N. Guo, Study on the corrosion electrochemistry behaviour and wear resistance of the arc thermal sprayed Zn-Al alloy coating, J. Mater. Res. Technol., 24 (**2023**), 8414–8428, doi:10.1016/j.jmrt.2023.05.109

[23] I. M. Chohan, A. Ahmad, N. Sallih, N. Bheel, W. M. Salilew, A. H. Almaliki, Effect of seawater salinity, pH, and temperature on external corrosion behaviour and microhardness of offshore oil and gas pipeline: RSM modelling and optimization, Sci. Rep., 14 (**2024**) 1, 18, doi:10.1038/s41598-024-67463-2

[24] L. Zhang, W. Chen, Q. Zhang, Z. Wang, Fracture failure analysis of traction transformer oil pump flange, Eng. Fail. Anal., 165 (**2024**), 108804, doi:10.1016/j.engfailanal.2024.108804

[25] J. C. Lu, Z. B. Wang, H. X. Hu, Y. G. Zheng, Understanding localized corrosion mechanism of 90/10 copper-nickel alloy in flowing NaCl solution induced by partial coverage of corrosion products films, Corrosion Sci., 227 (**2024**) 15, doi:10.1016/j.corsci.2023.111716

[26] C. T. Wang, M. F. Hassanein, M. M. Li, Numerical simulation of oil and gas pipeline corrosion based on single- or coupled-factor modeling: A critical review, Nat. Gas Ind. B, 10 (**2023**) 5, 445–465, doi:10.1016/j.ngib.2023.08.001

[27] D. Z. Xie, T. T. Wang, J. H. Ben, T. He, G. X. Chai, D. C. Wang, Mathematic modeling of the salt deposits growing on the tubing during debrining for gas storage salt cavern, J. Energy Storage, 55 (**2022**) 12, doi:10.1016/j.est.2022.105754

[28] X. Y. Miao, H. Zhao, Novel method for residual strength prediction of defective pipelines based on HTLBO-DELM model, Reliab. Eng. Syst. Saf., 237 (**2023**) 14, doi:10.1016/j.ress.2023.109369

[29] H. Ma, W. Zhang, Y. Wang, Y. Ai, W. Zheng, Advances in corrosion growth modeling for oil and gas pipelines: A review, Process Safety and Environmental Protection, 171 (**2023**), 71–86, doi:10.1016/j.psep.2022.12.054

[30] Z. Guo, Q. Shi, Y. Wang, Investigating the serve life of common earthed materials based on evaluations of the soil corrosion in offshore areas of East China, J. Phys., Conf. Ser. (UK), 2720 (**2024**) 1, 012007, doi:10.1088/1742-6596/2720/1/012007

[31] Z. W. Zhang, J. C. Wang, J. H. Zhang, Y. F. Cheng, Modeling of the mechano-electrochemical effect at corrosion defect with varied inclinations on oil/gas pipelines, Pet. Sci., 18 (**2021**) 5, 1520–1529, doi:10.1016/j.petsci.2021.08.012

[32] G. Mubarak, I. Gadala, I. Barsoum, A. AlFantazi, Numerical investigation of the mechano-electro-chemical effect of X100 buried pipelines with pre-existing corrosion defects, Heliyon, 9 (**2023**) 12, e22440, doi:10.1016/j.heliyon.2023.e22440